

Available online at www.sciencedirect.com

jmr&t
Journal of Materials Research and Technology
www.jmrt.com.br



Original Article

Effect of W content on the microstructure and properties of Cu-Fe alloy



Boxue Song^a, Tianbiao Yu^{a,*}, Xingyu Jiang^b, Wenchao Xi^a, Xiaoli Lin^a

^a Northeastern University, China

^b Shenyang University of Technology, China

ARTICLE INFO

Article history:

Received 16 October 2019

Accepted 7 April 2020

Available online 13 May 2020

Keywords:

Cu-Fe alloy

Liquid separation

Phase field

Wear resistance

Laser cladding

Metallurgy

ABSTRACT

The relationship between the microstructure and properties of laser-clad Cu-Fe alloys with different W contents was investigated. As the content of W increased, the size of the Fe core free in the Fe-rich region first decreased and then increased. In addition, almost all the W condensed in the Fe-rich region. The calculations verified that the Fe core in the molten pool was mainly driven by the Marangoni motion, and the phase field was used to simulate the nucleation and diffusion of the Fe cores inside the molten pool, revealing the formation process of the Fe-rich region. The addition of W was also beneficial in improving the wear resistance of the Cu-Fe alloy. When the W content was increased to 30%, the coefficient of friction of the alloy was reduced by 13%.

© 2020 The Author(s). Published by Elsevier B.V. This is an open access article under the CC BY-NC-ND license (<http://creativecommons.org/licenses/by-nc-nd/4.0/>).

1. Introduction

Copper is widely used in the industrial field due to its high electrical conductivity, thermal conductivity, and ductility [1–5]. However, due to its low hardness and poor abrasion resistance, its application in high-strength environments is severely limited [6]. To avoid this limitation, a variety of copper alloys were made, and different trace elements were added to improve performance.

Cu-Fe alloys are well-known as immiscible alloys with metastable miscible gaps, which cause Cu-Fe mixed solution to separate under a certain degree of subcooling [7–11].

Certain monotectic alloys, such as Cu-Co [12–15], exhibit similar characteristics, thereby deeming them ideal materials for electronic packaging, soft magnetic materials, and automotive bearings applications. In addition, miscible Cu-Fe alloys are inexpensive and have great potential and large-scale applications in the above-mentioned fields. However, Cu-Fe alloys undergo severe component segregation during solidification, which adversely affects their alloy properties and limits their application [16–18]. At present, Cu-Fe alloys are prepared by gas atomization spraying, electromagnetic suspension, microgravity dropper, and laser cladding [19–24]. Studies have shown that the liquid phase separation inside the Cu-Fe alloy is mainly dependent on the Stokes motion (affected by gravity) and the Marangoni motion (affected by the concentration gradient and temperature gradient). Under the first three process conditions, the solidification process of the Cu-Fe mixed solution is greatly affected by the Stokes motion

* Corresponding author.

E-mail: nightwaltz.harold@foxmail.com (T. Yu).

<https://doi.org/10.1016/j.jmrt.2020.04.031>

2238-7854/© 2020 The Author(s). Published by Elsevier B.V. This is an open access article under the CC BY-NC-ND license (<http://creativecommons.org/licenses/by-nc-nd/4.0/>).

and causes severe segregation. Although studies have been conducted to suppress such segregation, this phenomenon cannot be eliminated. Laser cladding, as an emerging rapid solidification technology, is becoming an ideal method for producing immiscible Cu-Fe alloys. Under rapid solidification conditions (cooling rate of 10^5 – 10^7 K/s), the laser can produce a high-speed convection motion inside the molten metal pool [25–29]. The surface tension- and temperature gradient-driven Marangoni convection effect is much larger than the gravity-driven Stokes motion, such that the heat and solute transport inside the molten pool is solely affected by the Marangoni motion, thus providing new means for the preparation of copper-iron alloys.

Chemical components also play an important role in controlling the properties and microstructure of Cu-Fe alloys. Zhou et al. [30] studied the effect of Al content on the solidification structure of the Cu-Fe alloy. It was pointed out that the main diffraction peak of ϵ -Cu phase weakened with the increase of Al content, but an increase in the main diffraction peak of the α -Fe phase and in Al was promoted. More Cu was deposited in the Fe-rich particles, improving the electrochemical resistance. Zhou et al. [31] pointed out that the addition of Si resulted in Cu_p and Fe_p coarsening, which increased the area percentage of the Fe-rich layer in the alloy and induced the in situ formation of the intermetallic compound Fe_3Si . Wang et al. [32] studied the solidification structure of the Fe-Cu-Sn ternary alloy under different degrees of subcooling and found that the Sn solute distribution curve of the Fe-rich and Cu-rich shells was slightly different from the droplet diameter in the core-shell structure. Dai et al. [15] successfully fabricated self-assembled Cu-Fe-Ni-Cr-Si immiscible alloys by laser induction cladding, which exhibited high saturation magnetization and low coercivity.

W and its carbides and boride, have high melting points, high hardness, and good wear resistance. In addition, they are widely used as strengthening phases of various alloys [33–35]. However, the properties and solidification morphology of the Cu-Fe-W ternary alloys have not been reported so far. In this study, a mixed alloy powder composed of Fe-based alloy powder, Cu, and W was used as the material, and Cu-Fe alloys with different W contents were prepared by laser cladding. The solidification morphology and its properties were measured and analyzed in detail. In addition, the phase-field model was applied to reveal the liquid phase separation kinetics of the immiscible alloy and its final evolution.

2. Experiments

The mixed alloy powder used in this study consists of three parts. The first part is Fe-based alloy powder of grade RCF103 (Table 1), which was purchased from Nanjing Zhongke Raycham Laser Technology Co., Ltd. The second part is a pure copper powder (99.9% purity), and the third part is pure tung-

Table 2 – Chemical composition of the mixed powder (wt%).

	RCF103	Cu	W
$\text{Cu}_{65}\text{Fe}_{35}$	35	65	0
$\text{Cu}_{58.5}\text{Fe}_{31.5}\text{W}_{10}$	31.5	58.5	10
$\text{Cu}_{52}\text{Fe}_{28}\text{W}_{20}$	28	52	20
$\text{Cu}_{45.5}\text{Fe}_{24.5}\text{W}_{30}$	24.5	45.5	30

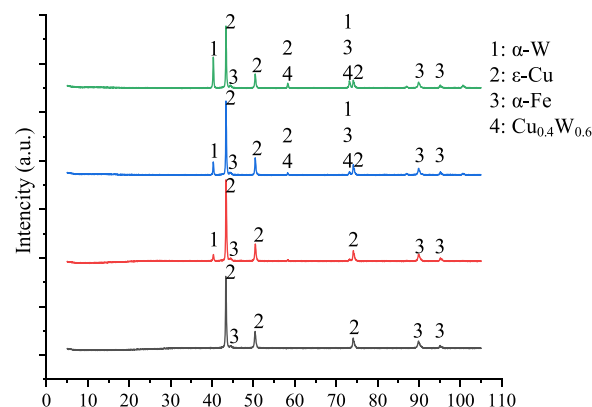


Fig. 1 – X-ray diffraction of the Cu-Fe alloy with different W contents.

sten powder (99.9% purity). The different powders are shown in Table 2.

The mixed alloy powder was dried for 5 h and then subjected to a laser cladding test with process parameters of laser power of 750 W, scanning speed of 8 mm/s, and powder feeding rate of 12.5 g/s. The surface of the obtained sample was polished with different meshes of sandpaper and, finally, the polished surface was etched with aqua regia. The solidified tissue was analyzed using an Oxford scanning electron microscope. The chemical composition of the alloy was analyzed by MPDDY2094 X-ray diffraction (XRD). The surface wear performance was measured using an MFT4000 surface property tester. A ball (GCr15, hardness of 60HRC) with a diameter of 5 mm was used as the counterpart. The test was performed for 50 min under a load of 100 N. The wear profile was measured using an OLS4000 laser microscope.

3. Results

3.1. XRD results

The XRD diffraction results of Cu-Fe alloys having different W contents are shown in Fig. 1. From the bottom to the top of the diffraction pattern, the content of W increases in turn. The obtained Cu-Fe alloy contains body-centered cubic α -Fe and face-centered cubic ϵ -Cu. The intensity of the diffraction

Table 1 – Chemical composition of RCF103 (wt%).

Components	C	Si	Mn	B	Cr	Ni	Mo	Nb	Fe
Proportion	0.07	1.1	0.4	0.23	15.2	5.1	1.0	0.31	Other

peak of W increased as the content increased, and a small amount of solid solution of Cu and W was also found in the alloy containing W.

3.2. Microstructure

The micro-morphology of Cu-Fe alloys with different W contents is shown in Fig. 2. Fig. 2a shows the microscopic morphology without W. An obvious separation state was observed in the Cu-rich and Fe-rich regions, specifically the dispersion of the Fe-rich solute in the Cu matrix. The Fe-rich region in the cladding layer has a macroscopic irregular shape. At the same time, the distribution of W can be observed in Fig. 2b–d, indicating that W was uniformly distributed in the Fe-rich region.

Fig. 3 shows a macro-cross-sectional structure of the Cu-Fe alloy. Fig. 3 clearly reveals the existence of significant macrosegregation inside the Cu-Fe alloy. The large Fe-rich regions were distributed in a stripe-like manner in the Cu-rich matrix. At the same time, many Fe cores were uniformly distributed on the Cu-rich matrix. In addition, almost all the bright white W was concentrated in the Fe-rich region.

Fig. 4 shows the boundary between the Cu-rich matrix and the Fe-rich region of the Cu-free alloy without W and its energy-dispersive X-ray spectroscopy (EDS) results.

The Fe cores and a Cu-rich region containing Cr were formed during solidification of the Cu-Fe alloy without W. Irregular dendritic solidification was also observed inside the Fe core. In addition, the Fe core may also contain a small number of microcracks. Many small spherical Fe cores were also observed around the Fe-rich area, and the internal solidification structure was similar to the large Fe core.

Fig. 5 shows the solidified structure of the Fe-rich edge region. As compared to Fig. 4, Fig. 5 indicates that W solidified inside the Fe core, and almost no W was observed in the Cu-rich region. Although W did not solidify in the copper-rich region, the stability of the solidification interface in the Cu-rich region improved as the W content increased. When the W content reached 30%, a large number of columnar crystals were observed in the Cu-rich region.

Fig. 6 presents the size distribution of the spherical Fe core in the Fe-rich region. When W was not contained in the alloy, the average size of the spherical Fe core was 4.74 μm . In comparison, a W content of 10% reduced the average size of the spherical Fe core to 2.68 μm . When the W content continued to increase to 20 and 30%, the average size of the spherical Fe core increased to 3.83 and 3.59 μm , respectively. In addition, the Fe core size of the Cu-free alloy containing W exhibited a bimodal distribution. A finer Fe core distribution was observed with the addition of W. In other words, the size of the Fe core decreased, while the amount increased.

Fig. 7 shows the Fe core of $\text{Cu}_{52}\text{Fe}_{28}\text{W}_{20}$. Many white bright spots were clearly observed in the Fe core. The white bright spot was more clearly depicted with increasing Fe cores. The EDS analysis results presented in Fig. 7 indicate that the difference in elemental composition between the white bright spot represented by A and the dark spot represented by B was mainly reflected in the content of Cu. The Cu content

in the dark (15.57 wt%) was higher than the content at the white bright spot (11.68 wt%). In addition, the EDS results also indicated that the concentration of Cu in the Fe core greatly exceeded the equilibrium solid solubility of α -Fe, revealing the presence of a small amount of secondary liquid phase separation.

4. Discussion on liquid phase separation mechanism of the Cu-Fe-Wu ternary alloy

4.1. Liquid phase separation of Cu-Fe and influence of W

The molten pool produced by laser cladding has a very large degree of subcooling, such that the occurrence of liquid phase separation can be clearly observed. At the macroscopic level, the separation between the Fe-rich region and the Cu-rich matrix can be clearly observed (Fig. 3), indicating that the laser cladding process used in the experiment was not sufficiently undercooled, thus allowing sufficient time for Cu and Fe to separate from each other. According to Fig. 8, the primary γ -Fe phase preferentially nucleated and grew dendrites in the absence of W. Following the addition of W, the preferential nucleation resulted in the generation of α -W with significant nucleation dynamics. The supercooling formation at the solidification interface after nucleation ensured the occurrence of primary liquid phase separation. In addition, the liquid phase, which constitutes supercooling above ΔT_c , continued to separate into a Fe-rich phase and a Cu-rich phase. Under the Cu-Fe-W ternary system, the preferential nucleation of W was still in the Cu-Fe miscible alloy. Following primary liquid phase separation, W was repelled as a solute by the copper-rich phase and was eventually surrounded by the Fe-rich nucleus.

For metastable immiscible Cu-Fe alloys, liquid phase separation occurs when the degree of subcooling of the melt is greater than the subcooling degree ΔT_c of the component [30]. According to the phase diagram shown in Fig. 7 [22], the subcooling threshold of the composition of Cu in the range of 11.68–15.57% was significantly larger than that of the Cu-Fe alloy used in the experiment (the composition of Cu was from 45.5 to 65 wt%). The degree of subcooling in the primary liquid phase separation of Fe did not exceed the supercooling threshold of the Fe-rich phase, such that the separated Fe nucleus did not be immediately subcool into the miscible gap. Therefore, contrary to the past literature [36], only a very small amount of secondary liquid phase separation occurred inside the Fe core in this experiment, which is consistent with the measurement results in Fig. 7.

Given that the melting point of W is much higher than Fe, the addition of W resulted in internally filled Fe with already nucleated W during nucleation. Since the density of W was also much larger than that of Fe, and the inside of the molten pool flowed vigorously, W formed a function similar to flushing and stirring in the Fe-rich region. At the beginning of nucleation, many Fe nuclei shrank to a spherical shape due to surface tension and subsequently moved closer to each other and fused together to form an Fe-rich region. The movement inside the molten pool mainly included the Marangoni

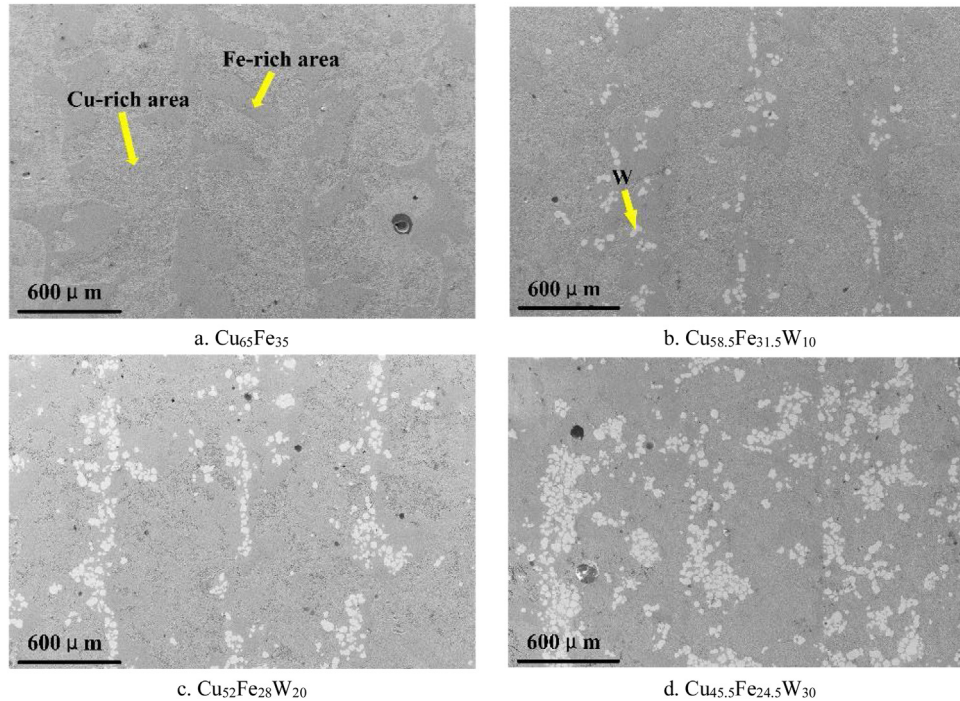


Fig. 2 – Microscopic morphology of the Cu-Fe alloy with different W contents.

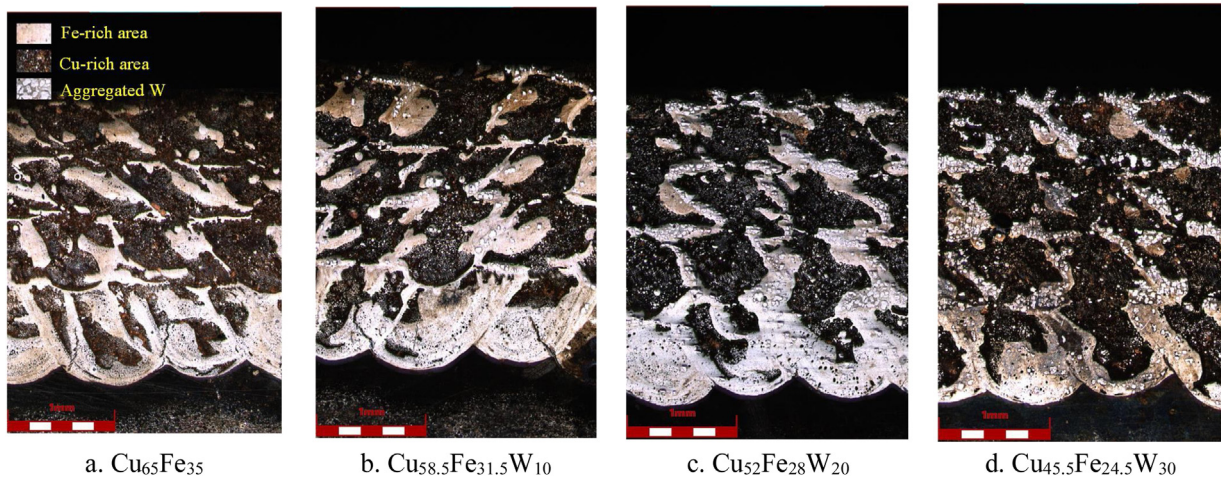


Fig. 3 – Cross-sectional macrostructure of the Cu-Fe alloy by laser cladding.

and Stokes movements. The speed of each movement can be expressed as [19]

$$v_m = \frac{-2r}{3(\mu_d + 2\mu_m)} \cdot \frac{\partial \sigma}{\partial T} \cdot G \quad (1)$$

$$v_s = \frac{2g\Delta\rho r^2}{3\mu_m} \cdot \frac{\mu_d + \mu_m}{3\mu_d + 2\mu_m} \quad (2)$$

where r is the radius of the iron-rich droplets; μ_d and μ_m are the viscosity of the liquid phase of the Fe-rich droplets and the Cu-rich matrix, respectively; g is gravity; $\Delta\rho$ is the density difference between the Fe-rich droplets and the Cu-rich matrix liquid phase; and σ is the interface energy. Previous lit-

erature [30] defined a competition coefficient and calculated the critical radius describing the spherical droplets driven by different motions. Under the critical radius, the velocity of the Fe core driven by Marangoni motion was close to that of Stokes motion. The radius of the Fe nucleus measured in this study was distributed below $10\ \mu\text{m}$, which was much smaller than the critical radius ($29.6\ \mu\text{m}$) in the literature [30], indicating that the Fe nucleus inside the molten pool was mainly driven by Marangoni motion. Although there is a large density difference between the Fe-rich region and the Cu-rich matrix, because the flow of the solution in the molten pool is controlled by the Marangoni motion, the main reason for macrosegregation should be the excessively small cooling rate, not the density difference.

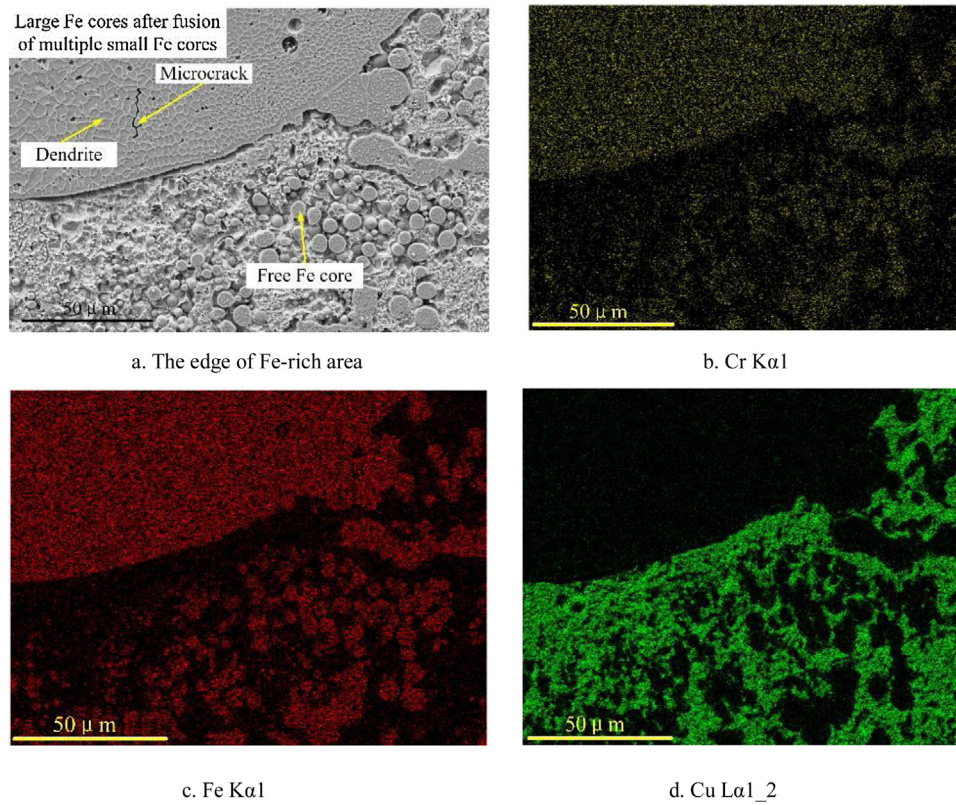


Fig. 4 – Edge of the Fe-rich region and its energy-dispersive X-ray spectroscopy (EDS) results.

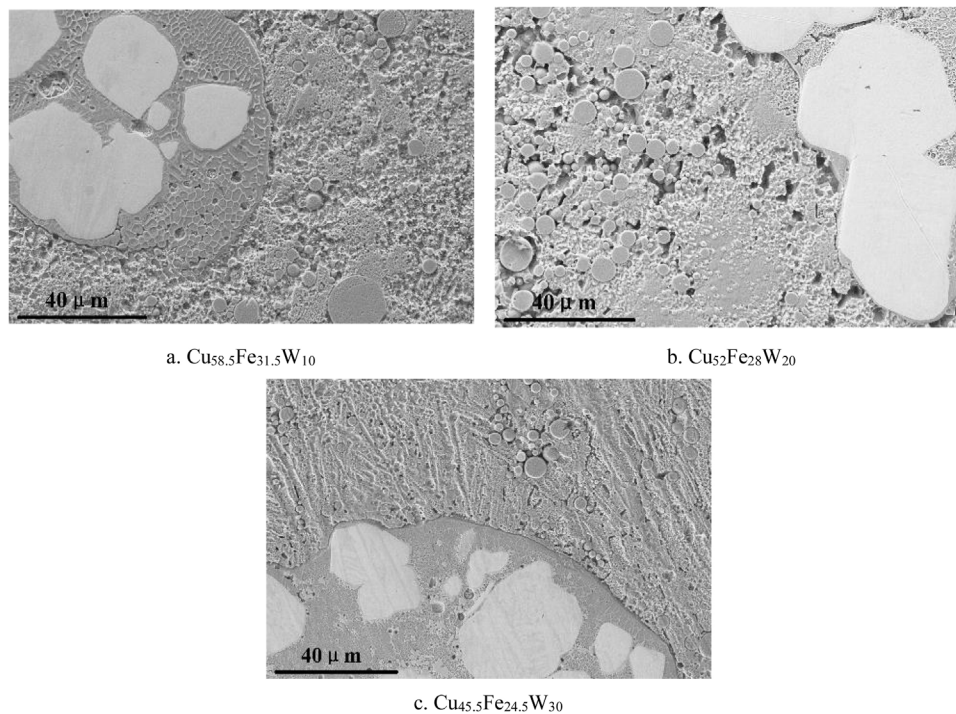


Fig. 5 – Edge of the Fe-rich region at different W contents.

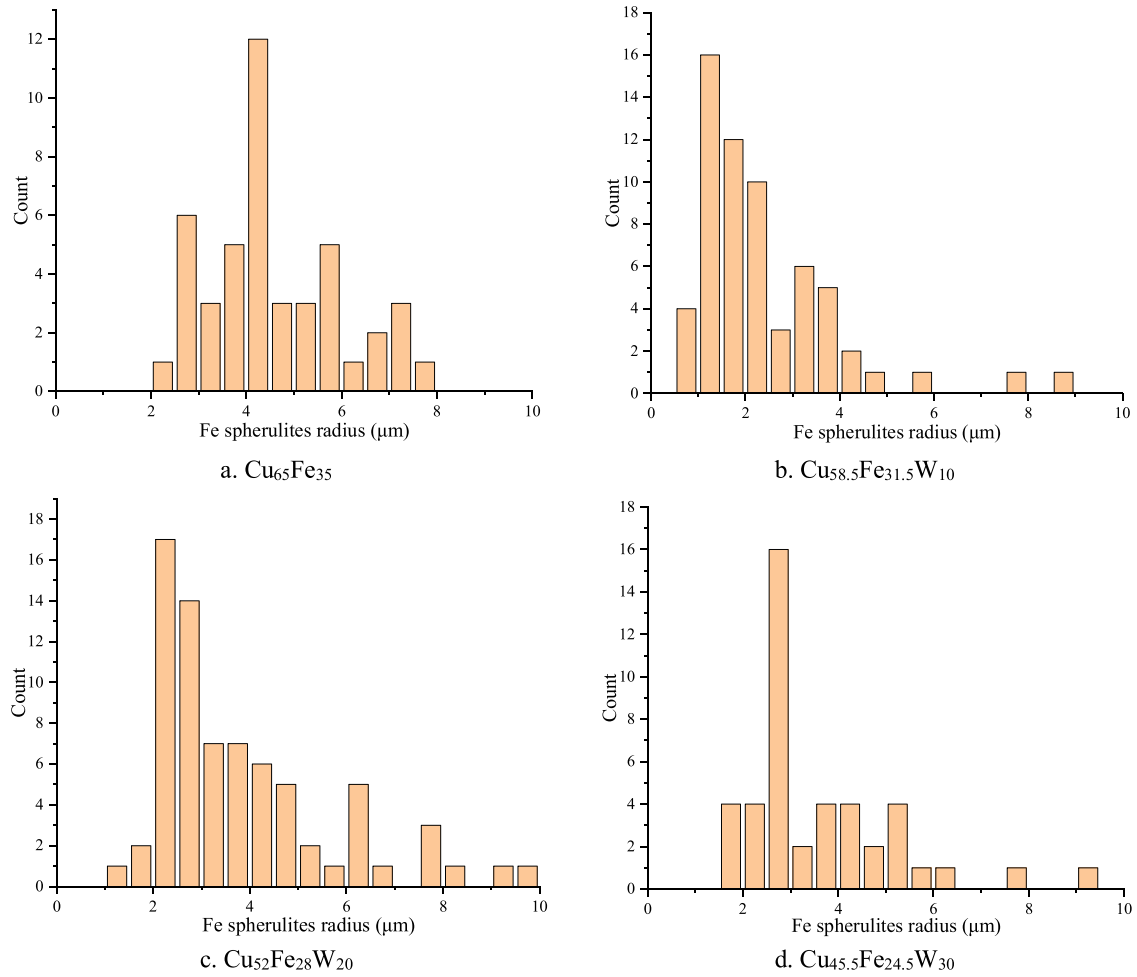


Fig. 6 – Distribution of Fe nuclei with different W contents.

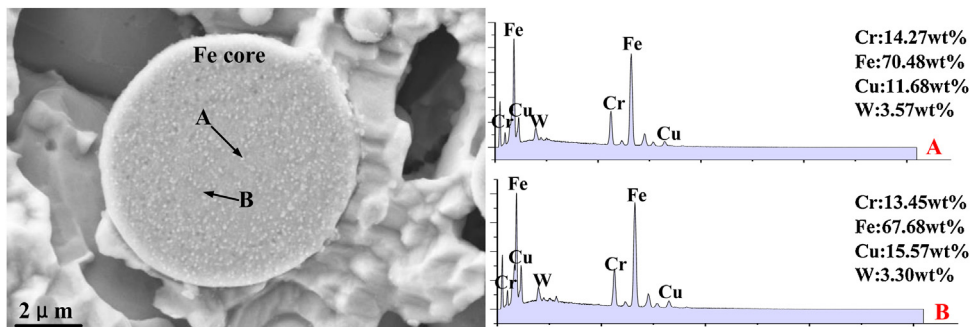


Fig. 7 – Micromorphology and elemental analysis of Fe nuclei in $\text{Cu}_{52}\text{Fe}_{28}\text{W}_{20}$.

4.2. Evolution of the Fe-rich and Cu-rich regions

As mentioned earlier, at the beginning of nucleation, many W nuclei were contained in the iron-rich melt, to which the Fe-rich melt separated from the Cu liquid phase. At the beginning of the liquid phase separation, numerous Fe nuclei were formed inside the melt, thereby resulting in the collision and fusion of different Fe nuclei. The evolution of the Fe nucleus

in the melt can be described by the Cahn–Hilliard-based total free energy governing equation:

$$F = \int_V \left[f(c) + \frac{1}{2} \kappa (\nabla c)^2 \right] dv \quad (3)$$

where κ is the gradient energy parameter, and c is the concentration. $f(c)$ is the chemical/volume energy and is expressed as

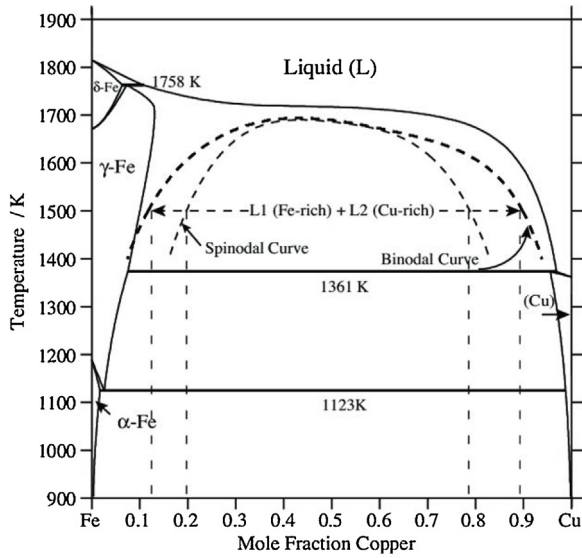


Fig. 8 – Cu-Fe binary phase diagram [22].

$$f(c) = Ac^2(1 - c)^2 \quad (4)$$

This is a simple phenomenological double-well potential. A is a positive constant that controls the size of the energy barrier between the two equilibrium phases, and the equilibrium concentration occurs at $c=0$ and $c=1$. It is assumed that in the three-dimensional region of discrete $N_x \times N_y \times N_z$, the discrete dot intervals in different directions are d_x , d_y , and d_z , respectively. The periodic boundary condition is set to

$$c_{0,j,k} = c_{N_x,j,k}, \quad c_{N_x+1,j,k} = c_{1,j,k} \quad (5)$$

$$c_{i,0,k} = c_{i,N_y,k}, \quad c_{i,N_y+1,k} = c_{i,1,k} \quad (6)$$

$$c_{i,j,0} = c_{i,j,N_z}, \quad c_{i,j,N_z+1} = c_{i,j,1} \quad (7)$$

where i , j , and k are the coordinate indices in the x -, y -, and z -directions, respectively. Substituting the differential of the free energy function into the Cahn–Hilliard equation yields a concentration field governing equation based on explicit Euler time integration:

$$\frac{c_{ijk}^{n+1} - c_{ijk}^n}{\Delta t} = \nabla^2 M \left(\frac{\partial F_{ijk}}{\partial c} \right)^n \quad (8)$$

where M is the dynamic parameter; Δt is the time step scale; and n is the n th time step. The partial differential form in parentheses on the right side of Eq. (8) is expressed as

$$\left(\frac{\partial F_{ijk}}{\partial c} \right)^n = \frac{df(c)}{dc} - \kappa \nabla^2 c_{ijk}^n \quad (9)$$

Discretization of Eq. (9) gives the total free energy variation of the system:

$$F_D = \sum_i \sum_j \sum_k f(c_{ijk}) + \frac{\kappa}{2} S \quad (10)$$

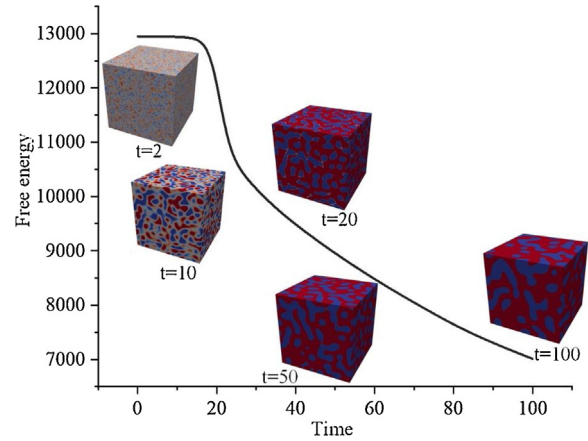


Fig. 9 – Movement of Fe nuclei over time and its free energy change.

$$S = \sum_i \sum_j \sum_k^{N_x-1, N_y-1, N_z-1} (c_{i+1,j,k} - c_{ijk})^2 + \sum_i \sum_j \sum_k^{N_x-1, N_y-1, N_z-1} (c_{i,j+1,k} - c_{ijk})^2 + \sum_i \sum_j \sum_k^{N_x-1, N_y-1, N_z-1} (c_{i,j,k+1} - c_{ijk})^2 \quad (11)$$

It is worth noting that in order to simplify the calculation, all physical parameters in the model are dimensionless parameters. Among them, dimensionless length, energy, and time are defined as

$$L_n = \sqrt{\frac{\kappa}{A}} \quad (12)$$

$$F_n = AL_n^3 \quad (13)$$

$$t_n = \frac{L_n^2 (c_p^e - c_m^e)^2}{MF_n} \quad (14)$$

where c_p^e and c_m^e are different phase equilibrium concentrations. The evolution rule of the Fe core is shown in Fig. 9.

According to Fig. 9, at the beginning of the phase separation, the microstructure was relatively fine and contained a large amount of precipitate. Over time, the Fe nuclei separated from the Cu matrix migrate through the phase boundaries, dissolved, and combined to form an Fe-rich region. The evolution of the Fe-rich region occurred during the Ostwald ripening process, and the smaller Fe nuclei were absorbed by the larger Fe core nucleus, resulting in a decrease in the total number of Fe nuclei over time. In addition, the total free energy of the separation process between the Cu-rich region and the Fe-rich region continuously decreased. In the early stage of separation, the free energy gradient was very large due to the continuous merging of many Fe nuclei. In the later stage, the expansion of the Fe-rich region and the free energy gradient slowed down due to the significant decrease in the amount of interface in the microstructure.

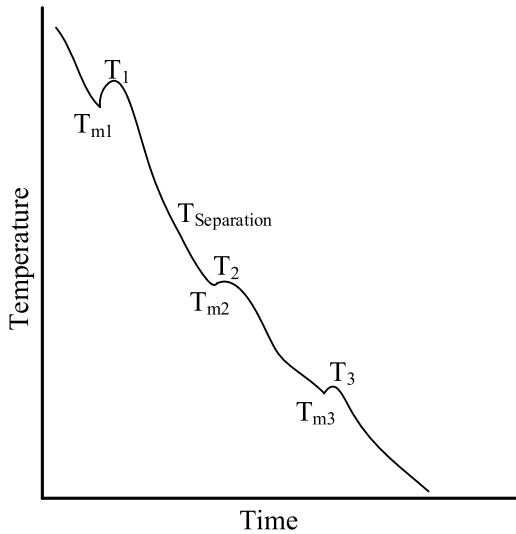


Fig. 10 – Schematic of cooling curve of Cu-Fe-W ternary alloy.

4.3. Solidification process of the molten pool

According to the cooling curve of a typical Cu-Fe alloy in the liquid phase separation, the schematic of cooling curve of the Cu-Fe-W ternary alloy can be similarly deduced (Fig. 10) [37]. During the cooling process, the nucleation of W first condensed, and the latent heat released during the nucleation raised the melt temperature to T1 due to the highest melting point.

Immediately after the melt was cooled to the liquid phase separation critical temperature, the Fe cores were generated in large quantities in the melt and collided with each other to form an Fe-rich region. In comparison, the already solidified W carried the inside of the Fe core. The latent heat released dur-

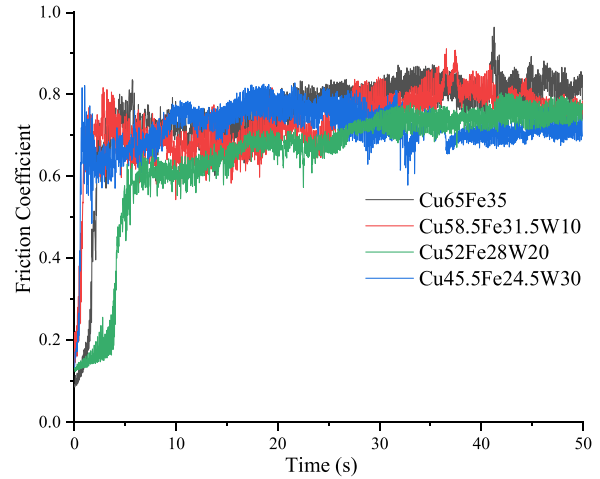


Fig. 11 – Wear test of the Cu-Fe alloy with different W contents.

ing the nucleation of Fe and Cu heated the melt temperatures to T2 and T3, respectively.

Under the strong Marangoni convection inside the melt, the first nucleation of W acted to a certain extent to stir the melt. This behavior hindered the fusion of the Fe core, resulting in a decrease in the average size of the Fe core. However, when there is a large amount of already nucleated W in the melt, the rate of movement of W inside the molten pool was lowered due to the higher density of W, such that more was deposited into the Fe-rich region. The hindrance of W to the Fe core was reduced, resulting in the re-increase of the average size of Fe cores. Therefore, a small amount of W was inferred to play a certain refinement effect on the microstructure of the Cu-Fe alloy, though a large amount of W weakened the refinement.

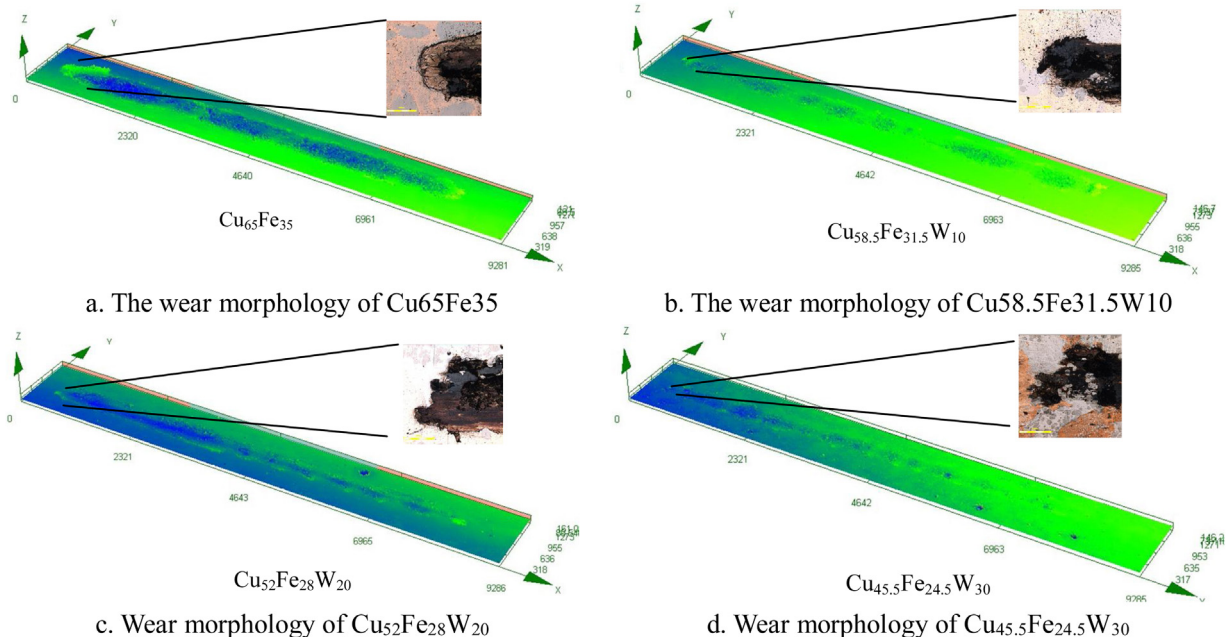


Fig. 12 – Three-dimensional (3D) display of the Cu-Fe alloy wear profile with different W contents.

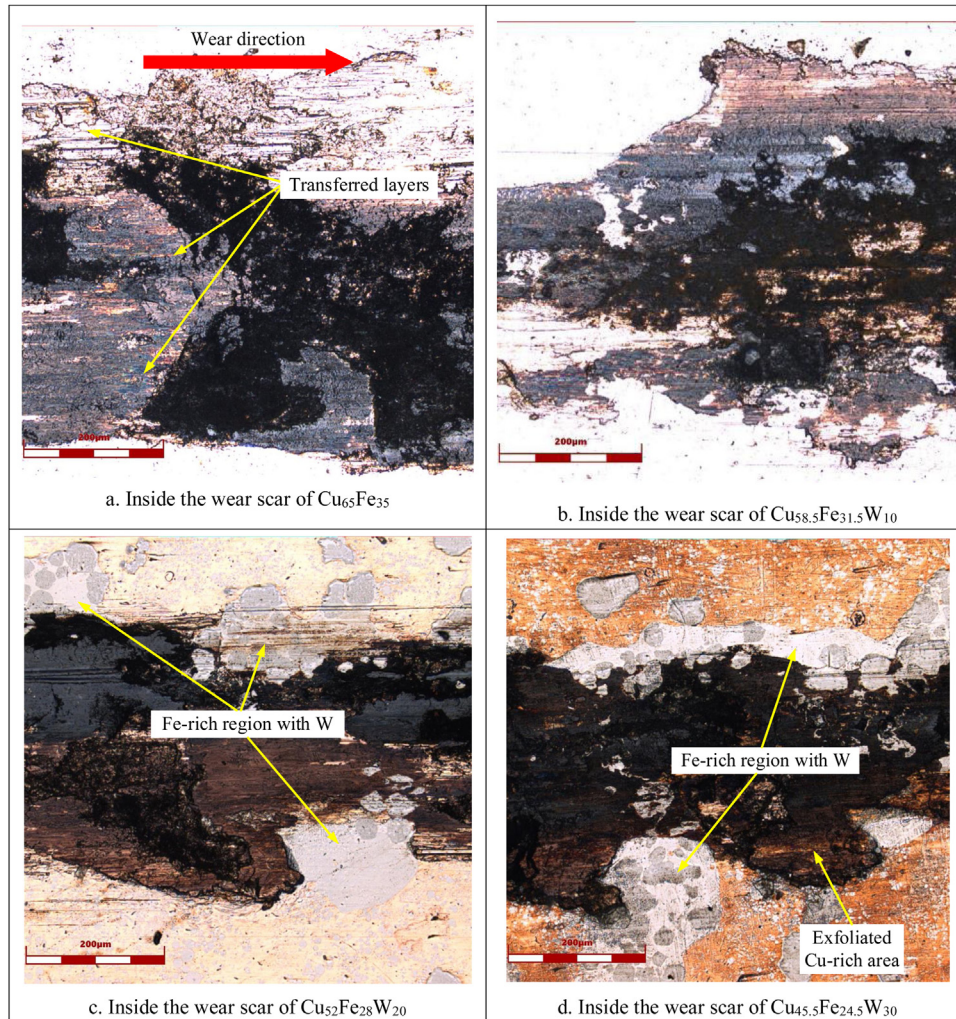


Fig. 13 – Internal conditions of the wear scars with different W contents.

4.4. Effect of W addition on the wear properties of the Cu-Fe alloy

Fig. 11 presents the friction and wear test of the alloy obtained in this study.

The Cu-Fe alloy had an average friction coefficient of 0.765, wherein the friction coefficient was reduced to 0.731 at a W mass fraction of 10%. In addition, the friction coefficient was further reduced to 0.717 at a W mass fraction of 20%. When W was increased to 30%, the coefficient of friction was reduced to 0.65. It is apparent that the friction coefficient of the Cu-Fe alloy decreased as the W content increased. In order to further study the wear morphology, the groove marks generated by friction were measured (Fig. 12).

The wear groove marks of $\text{Cu}_{65}\text{Fe}_{35}$ were most obvious, and the edge portion of the groove exhibited the obvious extrusion caused by plastic deformation. The addition of W smoothed the groove marks, and the extrusion effect at the edge portions was no longer obvious. Fig. 13 shows the inside of the wear scar with different W contents.

A clear tendency for adhesion on the wear scar surface was observed because $\text{Cu}_{65}\text{Fe}_{35}$ alloy has the lowest hardness. A

tear was apparent near the contact point between the grinding ball and the alloy surface. In addition, a part of the alloy material was pulled away and adhered to the grinding head, thereby resulting in material transfer. In other words, the $\text{Cu}_{65}\text{Fe}_{35}$ alloy and the grinding ball exhibited adhesive wear mechanism. Fig. 13a shows a part of the transfer layer. The transfer layer was mainly plate-shaped because the transferred fragments underwent plastic deformation as they continued to slide. The alloy hardness also increased following the addition of W. In Fig. 13b, a material transfer layer similar to that in Fig. 13a was not observed, and the wear mechanism gradually developed toward abrasive wear. As the W content increased, abrasive wear became more pronounced. When the W content was increased to 20%, the Cu-rich regions around the wear scars peeled off, whereas the iron-rich regions containing W were still observed. Because the stripped Fe filings continue to act as abrasives, the Cu-rich areas will be stripped more severely as the hardness of the alloy increases, as shown in Fig. 13d.

Improvements in the wear performance were presumably from the addition of W, which resulted in overall tissue refinement, whereas grain refinement improved the wear

resistance. Although the Fe nucleus contained supersaturated Cu in the absence of W, W was almost completely absorbed by the Fe nucleus after the addition of W, and the overall hardness of the Fe nucleus was strengthened. At the same time, as the W content increased, the supersaturated Fe contained in the Cu-rich region increased. In other words, the presence of W enhanced the solid solution of the Cu-rich and Fe-rich regions. In addition, the addition of W also increased the number of Fe nuclei, resulting in diffusion strengthening. The above reasons appeared to improve the wear resistance of the Cu-Fe alloy.

5. Conclusion

In this study, the phase separation mechanism and properties of laser clad Cu-Fe-W ternary alloy were discussed. The main conclusions include:

1. The Cu-Fe alloy underwent liquid phase separation in the molten pool to form a Cu-rich matrix phase and an Fe-rich region. Many spherical Fe nuclei were also scattered around the edge of the Fe-rich region. The size of the Fe core first increased and then decreased with the addition of W, while the number of Fe cores increased.
2. The solute inside the molten pool was mainly driven by the Marangoni movement. First, the nucleated W was absorbed by the later nucleated Fe cores, and then the Fe cores were then separated from the Cu-rich region. Different Fe cores collided with each other to form an Fe-rich region.
3. The supercooling degree of the Cu-Fe-W ternary alloy did not exceed the supercooling threshold of the Fe-rich phase in the primary liquid phase separation, thus generating a small amount of supersaturated Cu found in the Fe core.
4. The wear resistance of Cu-Fe alloy increased with the increase of W content. When the W content reached 20%, the wear morphology flattened and did not exhibit an obvious scratch.

Conflicts of interest

The authors declare no conflicts of interest.

Acknowledgments

This work was supported by [2016 Green Manufacturing System Integration Project of Ministry of Industry and Information Technology of China] under Grant [201675514] and Liaoning Provincial Key Laboratory of Large Equipment Intelligent Design and Manufacturing Technology under Grant [18006001]. And no potential conflict of interest was reported by the authors. We thank LetPub (www.letpub.com) for its linguistic assistance during the preparation of this manuscript.

REFERENCES

- [1] Boehlert C, Niinomi M, Ikeda M. Materials science and engineering C: introduction. *Mater Sci Eng C* 2005;25:247, <http://dx.doi.org/10.1016/j.msec.2004.12.008>.
- [2] Thompson LJ. Copper. *Vet. Toxicol. Basic Clin. Princ.* Third Ed; 2018. p. 425–7, <http://dx.doi.org/10.1016/B978-0-12-811410-0.00026-X>.
- [3] Sander B, Nizam A, Garrison LP, Postma MJ, Halloran ME, Longini IM. Economic evaluation of influenza pandemic mitigation strategies in the United States using a stochastic microsimulation transmission model. *Value Heal* 2009;12:226–33, <http://dx.doi.org/10.1111/j.1524-4733.2008.00437.x>.
- [4] Zortea T, Fraisse CW, Dewdney MM. Development of a web-based system to optimize copper fungicide application in citrus groves. *Appl Eng Agric* 2013;29:893–903, <http://dx.doi.org/10.13031/aea.29.10139>.
- [5] Richmond SJ, Gunadasa S, Bland M, MacPherson H. Copper bracelets and magnetic wrist straps for rheumatoid arthritis - analgesic and anti-inflammatory effects: a randomised double-blind placebo controlled crossover trial. *PLOS ONE* 2013;8, <http://dx.doi.org/10.1371/journal.pone.0071529>.
- [6] Haynes WM. *CRC Hdbk chemistry and physics. 97th Edition* CRC Press; 2016.
- [7] Kim DH, Kim WT, Park ES, Mattern N, Eckert J. Phase separation in metallic glasses. *Prog Mater Sci* 2013;58:1103–72, <http://dx.doi.org/10.1016/j.pmatsci.2013.04.002>.
- [8] Ratke L, Diefenbach S. Liquid immiscible alloys. *Mater Sci Eng R* 1995;15:263–347, [http://dx.doi.org/10.1016/0927-796X\(95\)00180-8](http://dx.doi.org/10.1016/0927-796X(95)00180-8).
- [9] Singh RN, Sommer F. Segregation and immiscibility in liquid binary alloys. *Rep Prog Phys* 1997;60:57–150, <http://dx.doi.org/10.1088/0034-4885/60/1/003>.
- [10] Mao Z, Sudbrack CK, Yoon KE, Martin G, Seidman DN. The mechanism of morphogenesis in a phase-separating concentrated multicomponent alloy. *Nat Mater* 2007;6:210–6, <http://dx.doi.org/10.1038/nmat1845>.
- [11] Chang HJ, Yook W, Park ES, Kyeong JS, Kim DH. Synthesis of metallic glass composites using phase separation phenomena. *Acta Mater* 2010;58:2483–91, <http://dx.doi.org/10.1016/j.actamat.2009.12.034>.
- [12] Bachmaier A, Schmauch J, Aboufadel H, Verch A, Motz C. On the process of co-deformation and phase dissolution in a hard-soft immiscible Cu-Co alloy system during high-pressure torsion deformation. *Acta Mater* 2016;115:333–46, <http://dx.doi.org/10.1016/j.actamat.2016.06.010>.
- [13] Wu C, Li M, Jia P, Liu R, Cui S, Geng H. Solidification of immiscible Al75Bi9Sn16 alloy with different cooling rates. *J Alloys Compd* 2016;688:18–22, <http://dx.doi.org/10.1016/j.jallcom.2016.06.275>.
- [14] Zhou S, Dai X, Xie M, Zhao S, Sercombe TB. Phase separation and properties of Cu-Fe-Cr-Si-C immiscible nanocomposite by laser induction hybrid cladding. *J Alloys Compd* 2018;741:482–8, <http://dx.doi.org/10.1016/j.jallcom.2018.01.184>.
- [15] Dai X, Xie M, Zhou S, Wang C, Yang J, Li Z. Formation and properties of a self-assembled Cu-Fe-Ni-Cr-Si immiscible composite by laser induction hybrid cladding. *J Alloys Compd* 2018;742:910–7, <http://dx.doi.org/10.1016/j.jallcom.2018.01.387>.
- [16] Dai X, Zhou S, Wang M, Lei J, Wang C, Wang T. Microstructure evolution of phase separated Fe-Cu-Cr-C composite coatings by laser induction hybrid cladding. *Surf Coat Technol* 2017;324:518–25, <http://dx.doi.org/10.1016/j.surfcoat.2017.06.032>.
- [17] Dai X, Zhou S, Wang M, Lei J, Xie M, Chen H, et al. Effect of substrate types on the microstructure and properties of Cu65Fe35 composite coatings by laser induction hybrid cladding. *J Alloys Compd* 2017;722:173–82, <http://dx.doi.org/10.1016/j.jallcom.2017.06.064>.

- [18] Zhao S, Zhou S, Xie M, Dai X, Chen D, Zhang LC. Phase separation and enhanced wear resistance of Cu88Fe12 immiscible coating prepared by laser cladding. *J Mater Res Technol* 2019;8:2001-10, <http://dx.doi.org/10.1016/j.jmrt.2018.12.018>.
- [19] Wang CP, Liu XJ, Ohnuma I, Kainuma R, Ishida K. Formation of immiscible alloy powders with egg-type microstructure. *Science* (80-) 2002;297:990-3, <http://dx.doi.org/10.1126/science.1073050>.
- [20] Wang CP, Liu XJ, Takaku Y, Ohnuma I, Kainuma R, Ishida K. Formation of core-type macroscopic morphologies in Cu-Fe base alloys with liquid miscibility gap. *Metall Mater Trans A Phys Metall Mater Sci* 2004;35 A:1243-53, <http://dx.doi.org/10.1007/s11661-004-0298-y>.
- [21] He J, Zhao JZ, Ratke L. Solidification microstructure and dynamics of metastable phase transformation in undercooled liquid Cu-Fe alloys. *Acta Mater* 2006;54:1749-57, <http://dx.doi.org/10.1016/j.actamat.2005.12.023>.
- [22] Shi RP, Wang CP, Wheeler D, Liu XJ, Wang Y. Formation mechanisms of self-organized core/shell and core/shell/corona microstructures in liquid droplets of immiscible alloys. *Acta Mater* 2013;61:1229-43, <http://dx.doi.org/10.1016/j.actamat.2012.10.033>.
- [23] Wang WL, Li ZQ, Wei B. Macro-segregation pattern and microstructure feature of ternary Fe-Sn-Si immiscible alloy solidified under free fall condition. *Acta Mater* 2011;59:5482-93, <http://dx.doi.org/10.1016/j.actamat.2011.05.022>.
- [24] Xia ZC, Wang WL, Luo SB, Wei B. Liquid phase separation and rapid dendritic growth of highly undercooled ternary Fe62.5Cu27.5Sn10 alloy. *J Appl Phys* 2015;117, <http://dx.doi.org/10.1063/1.4907214>.
- [25] Gan Z, Yu G, He X, Li S. Numerical simulation of thermal behavior and multicomponent mass transfer in direct laser deposition of Co-base alloy on steel. *Int J Heat Mass Transf* 2017;104:28-38, <http://dx.doi.org/10.1016/j.ijheatmasstransfer.2016.08.049>.
- [26] Song B, Yu T, Jiang X, Xi W. Numerical model of transient convection pattern and forming mechanism of molten pool in laser cladding. *Numer Heat Transf Part A Appl* 2019;75:855-73, <http://dx.doi.org/10.1080/10407782.2019.1608777>.
- [27] Zhao Y, Koizumi Y, Aoyagi K, Wei D, Yamanaka K, Chiba A. Molten pool behavior and effect of fluid flow on solidification conditions in selective electron beam melting (SEBM) of a biomedical Co-Cr-Mo alloy. *Addit Manuf* 2019;26:202-14, <http://dx.doi.org/10.1016/j.addma.2018.12.002>.
- [28] Tenner F, Berg B, Brock C, Klämpfl F, Schmidt M. Experimental approach for quantification of fluid dynamics in laser metal welding. *J Laser Appl* 2015;27:S29003, <http://dx.doi.org/10.2351/1.4906302>.
- [29] Galati M, Iuliano L. A literature review of powder-based electron beam melting focusing on numerical simulations. *Addit Manuf* 2018;19:1-20, <http://dx.doi.org/10.1016/j.addma.2017.11.001>.
- [30] Zhou S, Dai X, Xiong Z, Wu C, Zhang T, Zhang Z. Influence of Al addition on microstructure and properties of Cu-Fe-based coatings by laser induction hybrid rapid cladding. *J Mater Res* 2014;29:865-73, <http://dx.doi.org/10.1557/jmr.2014.64>.
- [31] Zhou S, Lei J, Xiong Z, Dai X, Guo J, Gu Z. Synthesis of Fe/Cu-Cu/Fe duplex composite coatings by laser cladding. *Mater Des* 2016;97:431-6, <http://dx.doi.org/10.1016/j.matdes.2016.02.125>.
- [32] Wang WL, Wu YH, Li LH, Zhai W, Zhang XM, Wei B. Liquid-liquid phase separation of freely falling undercooled ternary Fe-Cu-Sn alloy. *Sci Rep* 2015;5, <http://dx.doi.org/10.1038/srep16335>.
- [33] Peng H, Li R, Yuan T, Wu H, Yan H. Producing nanostructured Co-Cr-W alloy surface layer by laser cladding and friction stir processing. *J Mater Res* 2015;30:717-26, <http://dx.doi.org/10.1557/jmr.2015.28>.
- [34] Huang SW, Samandi M, Brandt M. Abrasive wear performance and microstructure of laser clad WC/Ni layers. *Wear* 2004;256:1095-105, [http://dx.doi.org/10.1016/S0043-1648\(03\)00526-X](http://dx.doi.org/10.1016/S0043-1648(03)00526-X).
- [35] Erfanmanesh M, Shoja-Razavi R, Abdollah-Pour H, Mohammadian-Semnani H. Influence of using electroless Ni-P coated WC-Co powder on laser cladding of stainless steel. *Surf Coat Technol* 2018;348:41-54, <http://dx.doi.org/10.1016/j.surfcoat.2018.05.016>.
- [36] Liu S, Jie J, Dong B, Guo Z, Wang T, Li T. Novel insight into evolution mechanism of second liquid-liquid phase separation in metastable immiscible Cu-Fe alloy. *Mater Des* 2018;156:71-81, <http://dx.doi.org/10.1016/j.matdes.2018.06.044>.
- [37] Liu N, Liu F, Chen Z, Yang G, Yang C, Zhou Y. Liquid-phase separation in rapid solidification of undercooled Fe-Co-Cu melts. *J Mater Sci Technol* 2012;28:622-5, [http://dx.doi.org/10.1016/S1005-0302\(12\)60107-8](http://dx.doi.org/10.1016/S1005-0302(12)60107-8).